Supporting Information:

Effusion nozzle for energy-efficient NO_x production in a rotating gliding arc plasma reactor

Senne Van Alphen*[1,2], Hamid Ahmadi Eshtehardi*[1,3], Jens Bogaerts[1], Helder Van Poyer[1], James Creel[1], Marie-Paule Delplancke[3], Rony Snyders[2,4] and Annemie Bogaerts[1]

[1]Research group PLASMANT, University of Antwerp, Department of Chemistry, Universiteitsplein 1, BE-2610 Wilrijk-Antwerp, Belgium.

[2] Research group ChIPS, Department of Chemistry, University of Mons, 20, Place du parc, 7000 Mons, Belgium.

[3]Research group 4MAT, Université Libre De Bruxelles, 50 Rossevelt Av., CP 165/63, 1050 Brussels, Belgium

[4]Materia Nova Research Center, 3 Avenue Nicolas Copernic, 7000 Mons, Belgium.

* Shared first author.

E-mail: senne.vanalphen@uantwerpen.be; Hamid.AhmadiEshtehardi@uantwerpen.be; annemie.bogaerts@uantwerpen.be

S.1. Experimental details

S.1.1 Experimental data for all operating conditions

Tables S.1. – S.3. Show the measured plasma power, NO and NO_2 concentration and Energy cost over a wide range of operating conditions, i.e., N_2/O_2 ratios ranging from 0.25 to 4, volumetric flow rates ranging from 1 to 10 L/min and electrical currents from 60 to 200 mA. Each experiment was performed three times for each condition. Figure S.1 shows the time evolution of the measured NO_x concentration over a 65 min measurement for the best performing condition in the main article, i.e. a 50/50 N_2/O_2 gas composition at a flow rate of 2 L/min in the steady arc regime (see figure 4 of the main article). As demonstrated by this figure, the NO_x production in the RGA is quite reliable,

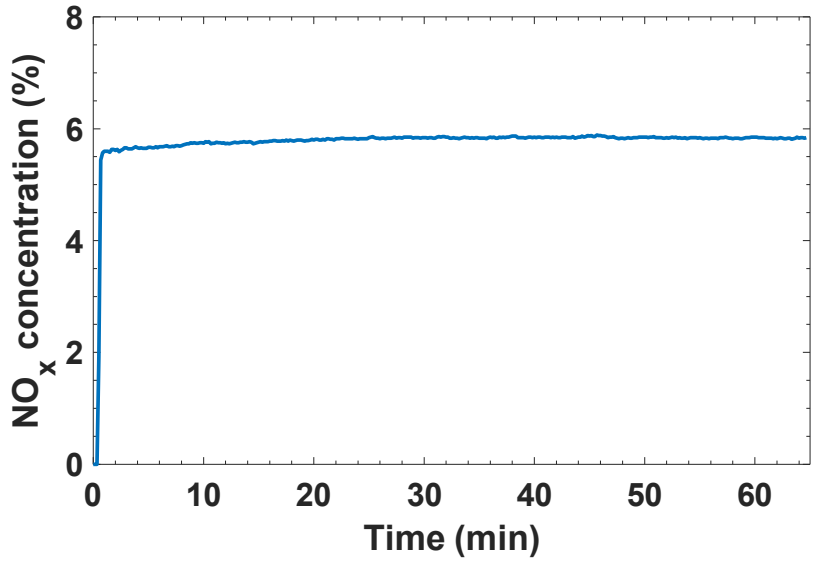

reaching a steady NO_x concentration within 30 seconds, which remains stable for the full 65 min time period. Given the very steady NO_x production, all experiments were performed over a 5 min time period.

Figure S.1: Time evolution of the measured NO_x concentration over a 65 min time period for a 50/50 N_2/O_2 gas composition at a flow rate of 2 L/min in the steady arc regime.

Table S.1. Total flow rate, applied current, plasma power, measured NO and NO_2 concentrations, and energy cost, as a function of gas composition, for the RGA with effusion nozzle operating in rotating arc regime

	Gas composition (N_2/O_2)	Flow rate (L/min)	Current (mA)	Plasma power (W)	Concentration (%)		Energy cost (MJ/mol)
					NO	NO_2	
Measurement 1	20/80	2	56	99.73	0.74	1.16	3.79
	40/60	2	56	97.88	1.01	1.60	2.71
	50/50	2	56	96.43	1.14	1.55	2.58
	60/40	2	60	101.66	1.28	1.49	2.64
	70/30	2	64	106.43	1.43	1.27	2.84
	80/20	2	69	110.66	1.52	0.82	3.41
Measurement 2	20/80	2	56	96.75	0.77	1.11	3.69
	40/60	2	56	99.07	1.1	1.70	2.55
	50/50	2	60	103.26	1.25	1.73	2.49
	60/40	2	63	107.81	1.41	1.63	2.56
	70/30	2	68	109.97	1.53	1.31	2.79
	80/20	2	69	110.46	1.56	0.82	3.34
Measurement 3	20/80	2	55	97.47	0.77	1.07	3.81
	40/60	2	58	100.16	1.1	1.64	2.63
	50/50	2	60	103.32	1.25	1.70	2.52
	60/40	2	63	107.56	1.41	1.58	2.59
	70/30	2	68	116.64	1.55	1.30	2.95
	80/20	2	69	111.78	1.59	0.87	3.27

Table S.2. Total flow rate, applied current, plasma power, measured NO and NO_2 concentrations, and energy cost as a function of gas composition, for the RGA with effusion nozzle operating in steady arc regime

	Gas composition (N_2/O_2)	Flow rate (L/min)	Current (mA)	Plasma power (W)	Concentration (%)		Energy cost (MJ/mol)
					NO	NO_2	
Measurement 1	20/80	2	130	205.26	1.15	3.36	3.28
	40/60	2	135	214.27	1.52	4.01	2.79
	50/50	2	135	203.42	1.80	4.16	2.45
	60/40	2	135	188.81	1.98	3.54	2.46
	70/30	2	135	172.56	2.18	2.74	2.53
	80/20	2	135	155.85	2.25	1.64	2.89
Measurement 2	20/80	2	135	207.19	1.15	3.40	3.28
	40/60	2	135	219.13	1.55	4.15	2.77
	50/50	2	135	202.18	1.76	4.09	2.49
	60/40	2	135	188.58	1.97	3.55	2.46
	70/30	2	135	171.76	2.16	2.70	2.55
	80/20	2	135	158.41	2.26	1.64	2.51
Measurement 3	20/80	2	135	213.61	1.15	3.39	3.38
	40/60	2	135	216.13	1.56	4.29	2.66
	50/50	2	135	209.11	1.76	4.09	2.57
	60/40	2	135	185.95	1.98	3.53	2.43
	70/30	2	135	169.33	2.18	2.69	2.51
	80/20	2	135	162.48	2.27	1.60	3.03

Table S.3. Total flow rate, applied current, plasma power, measured NO and NO_2 concentrations, and energy cost, as a function of gas composition, for the RGA without effusion nozzle operating in rotating arc regime

	Gas composition (N_2/O_2)	Flow rate (L/min)	Current (mA)	Plasma power (W)	Concentration (%)		Energy cost (MJ/mol)
					NO	NO_2	
Measurement 1	20/80	2	60	102.64	0.81	1.07	3.94
	40/60	2	60	102.20	1.12	1.52	2.79
	50/50	2	60	100.60	1.25	1.48	2.66
	60/40	2	60	99.92	1.35	1.30	2.71
	70/30	2	65	94.96	1.47	1.07	2.69
	80/20	2	65	102.49	1.46	0.62	3.55
Measurement 2	20/80	2	60	104.42	0.85	1.11	3.84
	40/60	2	60	103.25	1.15	1.57	2.74
	50/50	2	60	103.03	1.27	1.54	2.64
	60/40	2	60	102.35	1.39	1.33	2.71
	70/30	2	64	104.33	1.49	1.02	2.99
	80/20	2	68	107.24	1.51	0.62	3.63
Measurement 3	20/80	2	60	101.51	0.83	1.08	3.83
	40/60	2	60	101.96	1.15	1.54	2.73
	50/50	2	60	102.34	1.28	1.49	2.66
	60/40	2	60	100.49	1.38	1.28	2.72
	70/30	2	64	112.98	1.48	1.03	2.23
	80/20	2	68	106.71	1.51	0.62	3.62

Table S.4. Total flow rate, applied current, plasma power, measured NO and NO_2 concentrations, and energy cost, as a function of gas composition, for the RGA without effusion nozzle operating in steady arc regime

	Gas composition (N_2/O_2)	Flow rate (L/min)	Current (mA)	Plasma power (W)	Concentration (%)		Energy cost (MJ/mol)
					NO	NO_2	
Measurement 1	20/80	2	135	204.33	1.2	3.15	3.38
	40/60	2	135	211.99	1.58	3.76	2.86
	50/50	2	135	226.28	1.80	3.64	2.99
	60/40	2	135	221.55	2.01	3.19	3.07
	70/30	2	135	195.73	2.19	2.48	3.02
	80/20	2	135	193.43	2.28	1.46	3.72
Measurement 2	20/80	2	135	217.61	1.19	3.02	3.72
	40/60	2	135	239.52	1.61	3.78	3.20
	50/50	2	135	231.71	1.82	3.63	3.06
	60/40	2	135	225.81	2.05	3.24	3.08
	70/30	2	135	214.70	2.21	2.45	3.31
	80/20	2	135	205.59	2.29	1.49	3.91
Measurement 3	20/80	2	135	224.90	1.18	2.99	3.88
	40/60	2	135	235.79	1.63	3.86	3.09
	50/50	2	135	225.05	1.83	3.70	2.93
	60/40	2	135	212.41	2.03	3.12	2.92
	70/30	2	135	208.78	2.23	2.47	3.20
	80/20	2	135	196.73	2.28	1.48	3.77

S.2.1 Diagnostic device specification, calibration and standard curves used for NO_x measurements

In all gas conversion experimental setups, diagnostic devices are always one of the key components for measuring the amounts of desired products in the outlet stream of the process. For quantitative analysis of the desired species (NO, NO_2), a non-dispersive infrared (NDIR) continuous gas analyzer (EMERSON-Rosemount X-STREAM enhanced XEGP) was used as the diagnostic device in our experiments. The NDIR analyzer is designed to continuously determine the concentration of NO and NO_2 in the flowing gaseous mixtures fed to the device. The measured concentrations can be extracted from the device in ppm or volume percent scales.

Like all other conventional diagnostic devices, NDIR needs to get regularly calibrated to achieve the best and most proper measuring results. The calibration procedure for the NDIR is in general consists of three different steps that are separately explained below:

Zero calibration is a requirement to set the zero point of the measurement for the device. In this step a background gas recommended by the producer company (in our case pure Nitrogen) is fed to the device and a zero-cal procedure will be followed according to the user manuals of the device.

Span calibration is the other important step in the calibration of the device to set the maximum point of measurement for the device. In this step a gaseous mixture with concentrations of 80 to 110% of the upper measuring range limit of the gas analyzer sensor is fed to the device and a span-cal procedure is followed according to the user manuals provided by the produces company

Generation of the standard curves is the third and the last step in the calibration procedure of the device. In this step different gaseous flows with different concentrations from zero to the upper measuring range limit of the gas analyzer are fed to the device and the measured values by the device is recorded. By plotting the measured values by the device as function of actual fed gaseous mixtures a standard curve is generated which can then be used for accurate measurements of the desired products in the outlet stream of the experimental reactor set-up. The standard curves used for NO and NO_2 measurements in our experiments are presented in figure S.2.

Sampling flowrate fed to the device is also important in accurate measurements of concentrations components in the outlet stream of the process. The recommended sample flowrate by the device producer company is 500 to 1000 SCCM. Based on the manuals of the device, a lower flow sample should not affect the measured values by the device but may result in an undesirable time lag in the measurements. However, according to our experiences, a lower flowrate results in an overestimation of the measured concentrations. Therefore, sampling flowrates in the range of 980 to 1000 SCCM were fed to the device in all experiments to measure the concentrations of the products as accurate as possible. It should also be noted that excessive sampling flowrates can produce increased cell pressurization which results in reading errors and damages the sensors.

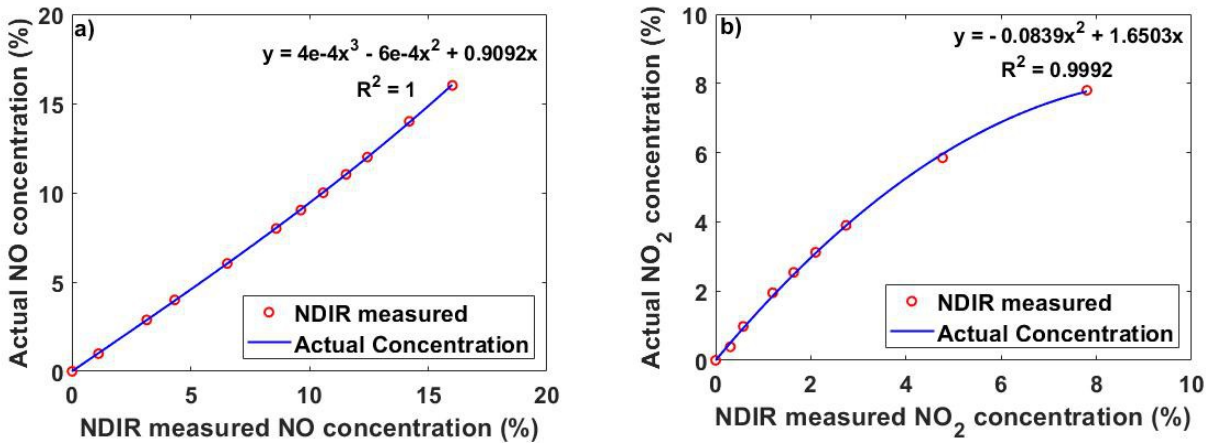

Figure S.2: Standard calibration curves used for measuring actual concentrations of a) NO and b) NO_2 using NDIR.

S.2. Modeling details

S.2.1. 3D Turbulent flow model

The RANS turbulent flow model solves the following mass continuity and momentum continuity Navier-Stokes equations for a Newtonian fluid.

(1) (2)

Where stands for the gas density, is the gas flow velocity vector, superscript T stands for transposition, is the gas pressure, is the dynamic viscosity and the turbulent viscosity of the fluid, is the turbulent kinetic energy, the unity tensor and the body force vector.

S.2.2. Fully coupled heat transfer model

The gas temperature is calculated by the following thermal balance equation:

(3)

Where stands for the mass density, for the isobaric heat capacity, is the temperature, the gas velocity field vector and the heat flux vector, which is calculated by:

(4)

Where is the surface emissivity, the Stefan-Boltzmann constant, k is the thermal conductivity, T_{amb} the ambient temperature, h the convective heat transfer coefficient and the unit vector normal to surfaces of the solid domains of the reactor. More details about how the convective heat transfer coefficient for heat transfer with the environment is calculated can be found in **section S.2.6** below.

In equation (4) Q is the heat source term, which is calculated by a step function in the axial direction, representing the arc length (i.e. 20 mm), and a Gaussian function in the radial direction representing the width of the arc (i.e. 2 mm). These arc dimensions are typical for gliding arc reactors [1–4], but as the arc length serves as an important input parameter for the model, a sensitivity analysis of the arc length on the modelling results is performed. Figure S.3 illustrates the effect of the arc length on the calculated gas temperature as obtained by the fully coupled heat transfer model for a reactor with an arc length of 20 and 10 mm for a plasma power of 199 W. This figure shows that a shorter arc concentrates the 199 W of plasma power in a smaller volume, leading to more gas heating and thus a higher gas temperature in the plasma. Figure S.4 shows the effect of this increased gas temperature on the calculated NO_x concentration as obtained by the quasi-1D chemical kinetics model for an arc length of 10, 12.5, 15, 17.5, 20, 22.5 and 25 mm. This figure shows that due to the higher gas temperatures in shorter arcs, a higher NO_x concentration is achieved. However, the figure also shows that the gain in NO_x formation becomes less significant as the arc length decreases. In short arcs the gas temperature in the center of the arc becomes so high that thermal NO_x decomposition becomes more dominant than NO_x formation reactions. The figure also shows that for the chosen arc length of 20 mm, an error of ± 0.5% in NO_x concentration is implemented in the model if the arc length is actually 2.5 mm longer or shorter, which is an acceptable sensitivity for the purpose of this model.

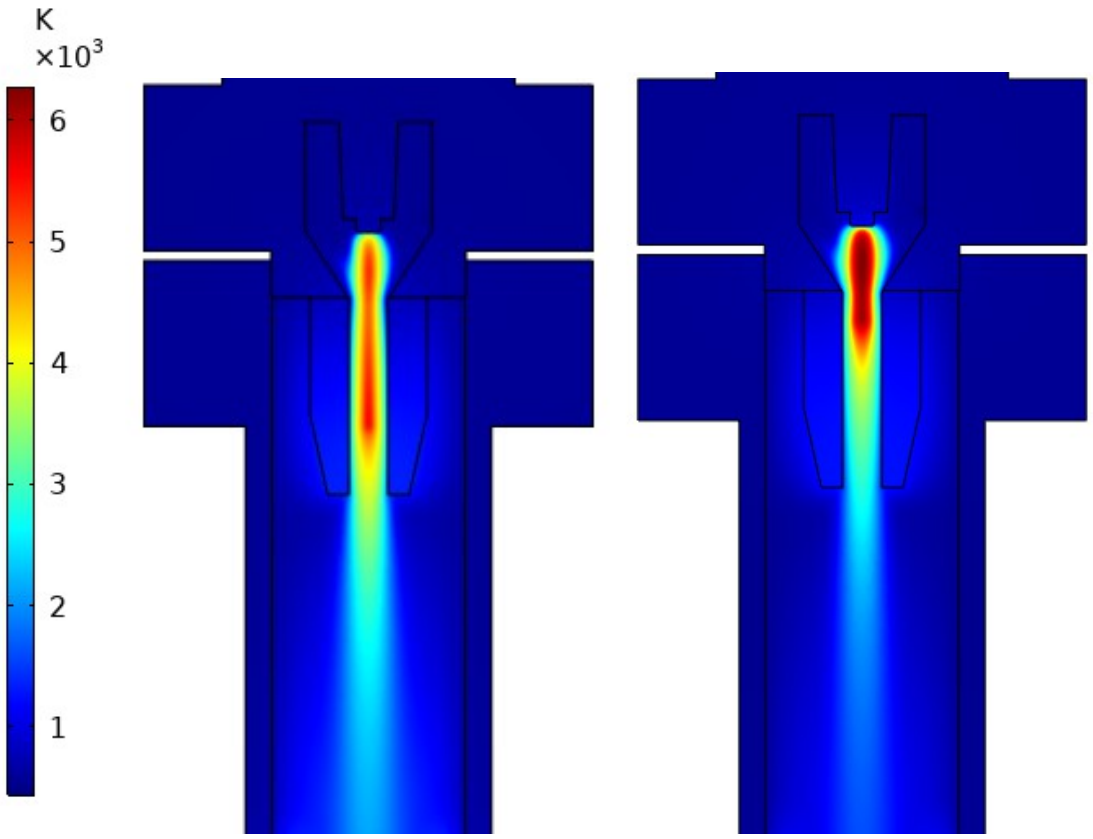

Figure S.3: Calculated gas temperature in the reactor without effusion nozzle for a plasma power of 199 W for an arc length of a) 20 mm and b) 10 mm, as obtained from the 3D fully coupled heat-transfer model.

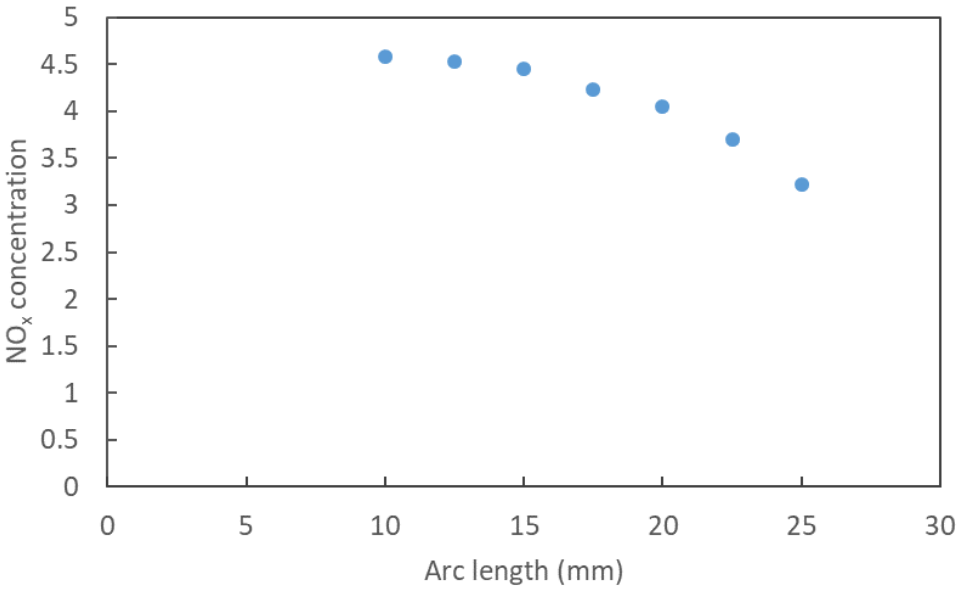

As explained in the main paper, the heating by the arc is calculated by the measured plasma power minus the power needed to produce the measured NO_x concentration (. The reason is that the formation of NO and NO_2

is endothermic (see equations (5,6)) and thus also requires power, which is thus not available anymore for gas heating. The procedure is as follows:

(5) (6)

(7)

(8) (9) (10)

Where and are the powers needed to form the measured NO and NO_2 concentrations, and are these measured NO and NO_2 concentrations, and and are the reaction enthalpies of reactions (5,6), respectively [6]. Hence, we assume that the remaining power goes to heating, which is only an approximation, because some part of the plasma power will also go to other reactions in the gas mixture, besides NO_x formation. However, most of these reactions in the end also lead to NO_x, [2,7], so we believe this approach is reasonable.

S.2.3. Material properties used in the models

The material properties used in the 3D turbulent gas flow model and the fully coupled heat transfer model are adopted from the COMSOL 5.6 material database for air and iron alloys [8]. For material properties of stainless steel, the iron alloy 304 [solid, oxidized] was used. **Tables S.1 and S.2** show the temperature dependencies of these properties for air and stainless steel, respectively. For stainless steel, instead of an interpolation, the material properties were defined using a piecewise function, and the surface emissivity of the stainless steel was taken to be 0.8, because the experiments revealed that the exhaust was quite oxidized.

For the fully coupled heat transfer model, an ambient temperature, $T_{amb,}$ of 293.15 K was used. In the tables below, T stands for the temperature, ρ the gas density, C_p the specific heat capacity at constant pressure, μ the dynamic viscosity, k the thermal conductivity, and σ the electrical conductivity.

Table S.1: *Temperature dependency of the properties for air in the 3D turbulent flow model, 3D thermal plasma model, and fully coupled heat transfer model.*

T (K)	ρ (kg m^{-3})	C_p (J kg^{-1} K^{-1})	$\mu\,(Pa.s)$	k (W m^{-1} K^{-1})
500	7.021E-01	1.047E+03	2.706E-05	4.138E-02
600	5.851E-01	1.069E+03	3.085E-05	4.824E-02
700	5.015E-01	1.086E+03	3.445E-05	5.497E-02
800	4.388E-01	1.103E+03	3.790E-05	6.160E-02
900	3.900E-01	1.119E+03	4.123E-05	6.814E-02
1000	3.510E-01	1.135E+03	4.446E-05	7.460E-02
1100	3.191E-01	1.151E+03	4.760E-05	8.116E-02
1200	2.925E-01	1.167E+03	5.067E-05	8.764E-02
1300	2.700E-01	1.184E+03	5.368E-05	9.415E-02
1400	2.508E-01	1.201E+03	5.662E-05	1.007E-01
1500	2.340E-01	1.219E+03	5.952E-05	1.074E-01
1600	2.194E-01	1.237E+03	6.236E-05	1.142E-01
1700	2.065E-01	1.257E+03	6.515E-05	1.212E-01
1800	1.950E-01	1.278E+03	6.791E-05	1.285E-01
1900	1.848E-01	1.301E+03	7.062E-05	1.363E-01
2000	1.755E-01	1.328E+03	7.330E-05	1.451E-01

2100	1.671E-01	1.361E+03	7.595E-05	1.552E-01
2200	1.595E-01	1.403E+03	7.856E-05	1.675E-01
2300	1.525E-01	1.456E+03	8.115E-05	1.829E-01
2400	1.460E-01	1.527E+03	8.372E-05	2.026E-01
2500	1.400E-01	1.620E+03	8.627E-05	2.279E-01
2600	1.344E-01	1.741E+03	8.882E-05	2.602E-01
2700	1.291E-01	1.894E+03	9.136E-05	3.005E-01
2800	1.240E-01	2.084E+03	9.391E-05	3.496E-01
2900	1.192E-01	2.310E+03	9.648E-05	4.074E-01
3000	1.145E-01	2.569E+03	9.901E-05	4.724E-01
3100	1.099E-01	2.855E+03	1.017E-04	5.415E-01
3200	1.055E-01	3.151E+03	1.043E-04	6.101E-01
3300	1.012E-01	3.435E+03	1.070E-04	6.716E-01
3400	9.702E-02	3.679E+03	1.097E-04	7.191E-01
3500	9.303E-02	3.852E+03	1.125E-04	7.464E-01
3600	8.925E-02	3.927E+03	1.152E-04	7.500E-01
3700	8.571E-02	3.891E+03	1.179E-04	7.307E-01
3800	8.244E-02	3.750E+03	1.205E-04	6.935E-01
3900	7.944E-02	3.528E+03	1.231E-04	6.463E-01
4000	7.610E-02	3.264E+03	1.257E-04	5.978E-01
4100	7.422E-02	2.997E+03	1.282E-04	5.547E-01
4200	7.195E-02	2.758E+03	1.307E-04	5.216E-01
4300	6.987E-02	2.567E+03	1.331E-04	5.006E-01
4400	6.794E-02	2.432E+03	1.356E-04	4.926E-01
4500	6.614E-02	2.353E+03	1.379E-04	4.974E-01
4600	6.445E-02	2.330E+03	1.403E-04	5.147E-01
4700	6.284E-02	2.357E+03	1.426E-04	5.444E-01
4800	6.130E-02	2.433E+03	1.450E-04	5.867E-01
4900	5.982E-02	2.556E+03	1.473E-04	6.418E-01
5000	5.839E-02	2.725E+03	1.496E-04	7.105E-01
5100	5.698E-02	2.940E+03	1.519E-04	7.935E-01
5200	5.561E-02	3.202E+03	1.543E-04	8.917E-01
5300	5.425E-02	3.515E+03	1.566E-04	1.006E+00
5400	5.290E-02	3.818E+03	1.589E-04	1.137E+00
5500	5.156E-02	4.295E+03	1.612E-04	1.286E+00
5600	5.022E-02	4.767E+03	1.636E-04	1.452E+00

5700	4.888E-02	5.295E+03	1.660E-04	1.636E+00
5800	4.753E-02	5.880E+03	1.683E-04	1.837E+00
5900	4.617E-02	6.520E+03	1.707E-04	2.053E+00
6000	4.480E-02	7.212E+03	1.731E-04	2.283E+00
6100	4.343E-02	7.952E+03	1.755E-04	2.522E+00
6200	4.205E-02	8.730E+03	1.778E-04	2.767E+00
6300	4.066E-02	9.534E+03	1.802E-04	3.011E+00
6400	3.929E-02	1.035E+04	1.825E-04	3.248E+00
6500	3.792E-02	1.115E+04	1.848E-04	3.471E+00
6600	3.656E-02	1.192E+04	1.870E-04	3.670E+00
6700	3.524E-02	1.262E+04	1.892E-04	3.837E+00
6800	3.395E-02	1.323E+04	1.913E-04	3.963E+00
6900	3.270E-02	1.371E+04	1.933E-04	4.043E+00
7000	3.151E-02	1.403E+04	1.952E-04	4.070E+00
7100	3.038E-02	1.416E+04	1.970E-04	4.043E+00
7200	2.932E-02	1.411E+04	1.988E-04	3.964E+00
7300	2.832E-02	1.386E+04	2.005E-04	3.837E+00
7400	2.740E-02	1.343E+04	2.021E-04	3.670E+00
7500	2.655E-02	1.284E+04	2.037E-04	3.473E+00
7600	2.577E-02	1.213E+04	2.053E-04	3.256E+00
7700	2.506E-02	1.134E+04	2.069E-04	3.031E+00
7800	2.441E-02	1.051E+04	2.086E-04	2.806E+00
7900	2.382E-02	9.678E+03	2.102E-04	2.591E+00
8000	2.327E-02	8.871E+03	2.119E-04	2.390E+00
8100	2.278E-02	8.113E+03	2.136E-04	2.208E+00
8200	2.232E-02	7.426E+03	2.153E-04	2.046E+00
8300	2.190E-02	6.806E+03	2.171E-04	1.907E+00
8400	2.151E-02	6.268E+03	2.189E-04	1.788E+00
8500	2.114E-02	5.807E+03	2.207E-04	1.690E+00
8600	2.080E-02	5.428E+03	2.225E-04	1.611E+00
8700	2.048E-02	5.103E+03	2.243E-04	1.550E+00
8800	2.017E-02	4.857E+03	2.261E-04	1.504E+00
8900	1.988E-02	4.647E+03	2.279E-04	1.471E+00
9000	1.960E-02	4.497E+03	2.297E-04	1.451E+00
9100	1.933E-02	4.408E+03	2.315E-04	1.443E+00
9200	1.907E-02	4.327E+03	2.332E-04	1.443E+00

9300	1.882E-02	4.318E+03	2.349E-04	1.454E+00
9400	1.857E-02	4.302E+03	2.366E-04	1.471E+00
9500	1.833E-02	4.353E+03	2.382E-04	1.497E+00
9600	1.810E-02	4.418E+03	2.398E-04	1.529E+00
9700	1.787E-02	4.463E+03	2.413E-04	1.565E+00
9800	1.764E-02	4.605E+03	2.421E-04	1.609E+00
9900	1.742E-02	4.689E+03	2.441E-04	1.656E+00
10000	1.720E-02	4.867E+03	2.453E-04	1.709E+00
10100	1.698E-02	5.040E+03	2.465E-04	1.767E+00
10200	1.677E-02	5.158E+03	2.475E-04	1.826E+00
10300	1.656E-02	5.405E+03	2.485E-04	1.892E+00
10400	1.635E-02	5.632E+03	2.493E-04	1.962E+00
10500	1.614E-02	5.866E+03	2.500E-04	2.036E+00
10600	1.593E-02	5.996E+03	2.505E-04	2.108E+00
10700	1.573E-02	6.366E+03	2.509E-04	2.188E+00
10800	1.552E-02	6.647E+03	2.511E-04	2.272E+00
10900	1.532E-02	6.802E+03	2.512E-04	2.353E+00
11000	1.511E-02	7.215E+03	2.510E-04	2.442E+00
11100	1.491E-02	7.560E+03	2.507E-04	2.535E+00
11200	1.471E-02	7.902E+03	2.502E-04	2.630E+00
11300	1.450E-02	8.258E+03	2.495E-04	2.728E+00
11400	1.430E-02	8.398E+03	2.486E-04	2.820E+00
11500	1.410E-02	8.953E+03	2.475E-04	2.921E+00
11600	1.390E-02	9.381E+03	2.462E-04	3.026E+00
11700	1.370E-02	9.792E+03	2.446E-04	3.132E+00
11800	1.349E-02	1.022E+04	2.429E-04	3.240E+00
11900	1.329E-02	1.065E+04	2.409E-04	3.350E+00
12000	1.309E-02	1.093E+04	2.387E-04	3.449E+00
12100	1.289E-02	1.147E+04	2.363E-04	3.558E+00
12200	1.269E-02	1.199E+04	2.337E-04	3.669E+00
12300	1.249E-02	1.247E+04	2.309E-04	3.781E+00
12400	1.229E-02	1.296E+04	2.279E-04	3.892E+00
12500	1.209E-02	1.345E+04	2.248E-04	4.004E+00
12600	1.189E-02	1.395E+04	2.214E-04	4.114E+00
12700	1.170E-02	1.491E+04	2.178E-04	4.209E+00
12800	1.150E-02	1.532E+04	2.142E-04	4.316E+00

12900	1.130E-02	1.591E+04	2.103E-04	4.418E+00
13000	1.111E-02	1.641E+04	2.063E-04	4.520E+00
13100	1.092E-02	1.690E+04	2.023E-04	4.619E+00
13200	1.073E-02	1.738E+04	1.981E-04	4.714E+00
13300	1.054E-02	1.785E+04	1.938E-04	4.806E+00
13400	1.035E-02	1.830E+04	1.894E-04	4.893E+00
13500	1.017E-02	1.874E+04	1.850E-04	4.974E+00
13600	9.983E-03	1.916E+04	1.805E-04	5.051E+00
13700	9.803E-03	1.990E+04	1.759E-04	5.121E+00
13800	9.623E-03	2.024E+04	1.713E-04	5.174E+00
13900	9.448E-03	2.056E+04	1.667E-04	5.232E+00
14000	9.277E-03	2.084E+04	1.621E-04	5.283E+00
14100	9.108E-03	2.128E+04	1.576E-04	5.326E+00
14200	8.942E-03	2.145E+04	1.530E-04	5.362E+00
14300	8.780E-03	2.158E+04	1.485E-04	5.386E+00
14400	8.621E-03	2.166E+04	1.441E-04	5.407E+00
14500	8.466E-03	2.170E+04	1.397E-04	5.420E+00
14600	8.315E-03	2.170E+04	1.353E-04	5.425E+00
14800	8.024E-03	2.165E+04	1.311E-04	5.422E+00
14900	7.884E-03	2.156E+04	1.269E-04	5.411E+00
15000	7.749E-03	2.143E+04	1.228E-04	5.393E+00
15100	7.617E-03	2.126E+04	1.189E-04	5.359E+00
15200	7.489E-03	2.105E+04	1.150E-04	5.337E+00
15300	7.366E-03	2.080E+04	1.112E-04	5.299E+00
15400	7.246E-03	2.052E+04	1.075E-04	5.255E+00
15500	7.130E-03	2.020E+04	1.040E-04	5.206E+00
15600	7.018E-03	1.986E+04	1.006E-04	5.152E+00
15700	6.910E-03	1.949E+04	9.725E-05	5.094E+00
15800	6.806E-03	1.909E+04	9.405E-05	5.032E+00
15900	6.706E-03	1.867E+04	9.098E-05	4.966E+00
16000	6.609E-03	1.824E+04	8.803E-05	4.898E+00
16100	6.515E-03	1.779E+04	8.520E-05	4.829E+00
16200	6.425E-03	1.733E+04	8.249E-05	4.757E+00
16300	6.338E-03	1.686E+04	7.989E-05	4.685E+00
16400	6.255E-03	1.639E+04	7.742E-05	4.612E+00
16500	6.174E-03	1.592E+04	7.506E-05	4.540E+00

16600	6.097E-03	1.544E+04	7.282E-05	4.468E+00
16700	6.022E-03	1.497E+04	7.068E-05	4.397E+00
16800	5.950E-03	1.450E+04	6.866E-05	4.327E+00
16900	5.881E-03	1.403E+04	6.674E-05	4.258E+00
17000	5.814E-03	1.358E+04	6.492E-05	4.192E+00
17100	5.750E-03	1.313E+04	6.320E-05	4.127E+00
17200	5.688E-03	1.270E+04	6.158E-05	4.065E+00
17300	5.628E-03	1.227E+04	6.005E-05	4.005E+00
17400	5.570E-03	1.186E+04	5.861E-05	3.948E+00
17500	5.514E-03	1.148E+04	5.725E-05	3.894E+00
17600	5.460E-03	1.108E+04	5.598E-05	3.842E+00
17700	5.408E-03	1.071E+04	5.479E-05	3.794E+00
17800	5.358E-03	1.036E+04	5.367E-05	3.748E+00
17900	5.309E-03	1.002E+04	5.263E-05	3.705E+00
18000	5.262E-03	9.690E+03	5.165E-05	3.665E+00
18100	5.216E-03	9.380E+03	5.074E-05	3.628E+00
18200	5.171E-03	9.017E+03	4.990E-05	3.594E+00
18300	5.128E-03	8.798E+03	4.911E-05	3.562E+00
18400	5.088E-03	8.532E+03	4.838E-05	3.533E+00
18500	5.047E-03	8.280E+03	4.786E-05	3.508E+00
18600	5.007E-03	8.042E+03	4.724E-05	3.484E+00
18700	4.969E-03	7.818E+03	4.667E-05	3.463E+00
18800	4.931E-03	7.608E+03	4.614E-05	3.445E+00
18900	4.895E-03	7.410E+03	4.565E-05	3.429E+00
19000	4.859E-03	7.225E+03	4.521E-05	3.415E+00
19100	4.824E-03	7.052E+03	4.481E-05	3.403E+00
19200	4.790E-03	6.731E+03	4.444E-05	3.393E+00
19300	4.757E-03	6.595E+03	4.411E-05	3.385E+00
19400	4.731E-03	6.470E+03	4.381E-05	3.379E+00
19500	4.699E-03	6.355E+03	4.399E-05	3.376E+00
19600	4.668E-03	6.252E+03	4.375E-05	3.374E+00
19700	4.637E-03	6.159E+03	4.353E-05	3.374E+00
19800	4.607E-03	6.075E+03	4.335E-05	3.375E+00
19900	4.578E-03	6.002E+03	4.318E-05	3.378E+00
20000	4.549E-03	5.939E+03	4.304E-05	3.382E+00
20100	4.520E-03	5.886E+03	4.292E-05	3.388E+00

20200	4.493E-03	5.842E+03	4.282E-05	3.395E+00
20300	4.465E-03	5.808E+03	4.274E-05	3.404E+00
20400	4.438E-03	5.784E+03	4.268E-05	3.413E+00
20500	4.412E-03	5.769E+03	4.263E-05	3.424E+00
20600	4.385E-03	5.763E+03	4.260E-05	3.436E+00
20700	4.360E-03	5.767E+03	4.258E-05	3.449E+00
20800	4.334E-03	5.781E+03	4.257E-05	3.463E+00
20900	4.309E-03	5.804E+03	4.257E-05	3.478E+00
21000	4.284E-03	5.837E+03	4.259E-05	3.494E+00
21100	4.260E-03	5.879E+03	4.261E-05	3.511E+00
21200	4.236E-03	5.932E+03	4.264E-05	3.529E+00
21300	4.212E-03	5.995E+03	4.268E-05	3.548E+00
21400	4.188E-03	6.068E+03	4.272E-05	3.567E+00
21500	4.164E-03	6.151E+03	4.277E-05	3.587E+00
21600	4.141E-03	6.245E+03	4.282E-05	3.608E+00
21700	4.118E-03	6.350E+03	4.288E-05	3.630E+00
21800	4.095E-03	6.465E+03	4.293E-05	3.652E+00
21900	4.073E-03	6.731E+03	4.299E-05	3.675E+00
22000	4.050E-03	6.881E+03	4.305E-05	3.698E+00
22100	4.028E-03	7.043E+03	4.310E-05	3.722E+00
22200	4.006E-03	7.216E+03	4.315E-05	3.747E+00
22300	3.984E-03	7.402E+03	4.335E-05	3.772E+00
22400	3.962E-03	7.600E+03	4.339E-05	3.798E+00
22500	3.940E-03	7.811E+03	4.343E-05	3.824E+00
22600	3.918E-03	8.269E+03	4.346E-05	3.850E+00
22700	3.897E-03	8.519E+03	4.349E-05	3.877E+00
22800	3.875E-03	8.782E+03	4.350E-05	3.904E+00
22900	3.853E-03	9.057E+03	4.351E-05	3.932E+00
23000	3.836E-03	9.346E+03	4.350E-05	3.960E+00
23100	3.814E-03	9.649E+03	4.388E-05	3.986E+00
23200	3.793E-03	9.964E+03	4.385E-05	4.015E+00
23300	3.771E-03	1.029E+04	4.381E-05	4.043E+00
23400	3.749E-03	1.064E+04	4.375E-05	4.073E+00
23500	3.728E-03	1.099E+04	4.368E-05	4.102E+00
23600	3.706E-03		4.359E-05	4.132E+00
23700	3.684E-03		4.349E-05	4.161E+00

23800	3.663E-03		4.337E-05	4.192E+00
23900	3.641E-03		4.324E-05	4.222E+00
24000	3.619E-03		4.309E-05	4.252E+00

Table S.2: *Temperature dependency of the properties for stainless steel in the 3D turbulent gas flow model and fully coupled heat transfer model.*

ρ (kg m^{-3})		
Start T (K)	End T (K)	Function
4	93	7930.967 + 0.03300298 T 9.663581 10^{-4} $T^2$2.91717810^{-6} T^3
93	1700	7945.3330.1981948 T 3.713764 10^{-4} T^2 + 2.213069 10^{-7} T^3 5.12845610^{-11} T^4
Cp (J kg^{-1} K^{-1})		
Start T (K)	End T (K)	Function
4	14	4.80349978 1.97398861 T + 0.433444409 T^2 0.0314324757 T^3 + 8.32403453 10^{-4} T^4
14	47	0.224295746 + 0.760568357 T 0.0400750758 T^2 + 0.00218176061 T^3 0.0000183602372 T^4
47	128	8.9262753 2.90098686 T + 0.147079315 T^2 0.00125489708 T^3 + 3.41401137 10^{-6} T^4
128	310	270.215021 1.21051111 T + 0.0215156635 T^2 7.51184063 10^{-5} T^3 + 8.13679634 10^{-8} T^4
310	1311	109.207295 + 2.5717751 T 0.00652809855 T^2 + 7.78752439 10^{-6} T^3 4.16791252 10^{-9} T^4 + 8.09061335 10^{-13} T^5
k (W m^{-1} K^{-1})		
Start T (K)	End T (K)	Function
1	45	0.03740871 + 0.06460546 T + 0.003720604 T^2 0.00008390067 T^3 + 0.0000006006594 T^4
45	283	1.031521 + 0.1813807 T 0.001088656 T^2 + 0.000003411681 T^3 0.000000003988389 T^4
283	887	1.258169 + 0.1023945 T 0.0002189547 T^2 + 0.0000002312931 T^3 0.00000000008903937 T^4
σ (S m^{-1})		
Start T (K)	End T (K)	Function
4	1173	$\frac{1}{(1.750491\ 10^{-13}\ T^2 + 8.670423\ 10^{-10}\ T + 4.769612\ 10^{-7})}$

S.2.4. Heat transfer with the environment

The convective heat transfer coefficient of the reactor with the environment is calculated using Nusselt's number, which is the ratio of convective over conductive heat transfer at a boundary in a fluid. It's a dimensionless number and is calculated via the following formula:

(11)

Where h is the convective heat transfer coefficient, L is a characteristic length, and k it the thermal conductivity in the fluid. In our case, we have free convective heat transfer since we don't force the air to flow around the outside of the reactor. Therefore, Nusselt's number for the free convective heat transfer is a function of Prandtl's (Pr) and Grashof's (Gr) number, which themselves are also dimensionless numbers which can be calculated via the following formulas:

(12)

Where C_p is the specific heat capacity at constant pressure, the dynamic viscosity of the fluid, k the thermal conductivity in the fluid, g the standard acceleration of free fall, the coefficient of thermal expansion, the surface temperature, the bulk temperature of the gas, D the diameter of the cylinder or length of the plate, the kinematic viscosity, and Ra the Rayleigh number. Prandtl's number relates material characteristics and Grashof's number is the ratio of the buoyancy force over the viscous force acting on a fluid. All these dimensionless numbers are well known, and we can find a relationship between Nusselt's number and Prandtl's and Grashof's number [9,10]:

(13)

As the RGA from the outside consists of two geometrical shapes, a cylinder and a cuboid, two different relationships have to be used: one which describes the free convective heat transfer around a cylinder, and one which describes the free convective heat transfer across a plate, since the cuboid can be seen as 4 plates attached together. Filling these formula's in previous equation gives us the following formulas [9,10]:

Cylinder: (14)

Vertical plate: (15)

The last step that remains is inserting the material properties and calculate the convective heat transfer coefficient. For the diameter of the cylinder (see eq. (25), Gr), the outer diameter of the exhaust is used (25.2 mm), and for the length of the plates, L, the length across which the air flows across the planes of the cuboid is used (18.9 mm). To simplify things, we did not consider the temperature dependency of the physical properties used in these formulas. This results in a less accurate prediction of the heat transfer coefficient at larger temperatures, but as the heat transfer coefficient stays relatively low for the free convective heat transfer, this error remains limited. The used values for the physical properties were for air at 293.15 K and obtained from COMSOL Multiphysics 5.6 material database for air [8]. **Table S.3** shows the resulting convective heat transfer coefficients calculated using these formulas and they were implemented in COMSOL via an interpolation table.

Table S.3*: Convective heat transfer coefficients calculated with equations (14) and (15) above.*

T (K)	h (W m^{-2} K^{-1}) (cylinder)	h (W m^{-2} K^{-1}) (plates)

293.15	0.79	1.49
300	7.99	10.10
305	9.07	11.32
310	9.86	12.21
315	10.49	12.93
320	11.03	13.53
325	11.50	14.06
330	11.93	14.53
335	12.31	14.95
340	12.66	15.35
345	12.99	15.71
350	13.29	16.05
355	13.58	16.36
360	13.85	16.66
365	14.10	16.95
370	14.35	17.22
375	14.58	17.47
380	14.80	17.72
385	15.02	17.96
390	15.22	18.18
395	15.42	18.40
400	15.61	18.62
405	15.80	18.82
410	15.98	19.02
415	16.15	19.21
420	16.32	19.40
425	16.49	19.58
430	16.65	19.76
435	16.81	19.93
440	16.96	20.10
445	17.11	20.26
450	17.25	20.42
455	17.40	20.58
460	17.54	20.73
465	17.67	20.88
470	17.81	21.03

475	17.94	21.17
480	18.07	21.31
485	18.19	21.45
490	18.32	21.59
495	18.44	21.72
500	18.56	21.85
505	18.68	21.98
510	18.79	22.11
515	18.91	22.23
520	19.02	22.36
525	19.13	22.48
530	19.24	22.60
535	19.34	22.71
540	19.45	22.83
545	19.55	22.94
550	19.66	23.05
555	19.76	23.17
560	19.86	23.27
565	19.96	23.38
570	20.05	23.49
575	20.15	23.59
580	20.24	23.70
585	20.34	23.80
590	20.43	23.90
595	20.52	24.00
600	20.61	24.10
605	20.70	24.20
610	20.79	24.30
615	20.88	24.39
620	20.97	24.49
625	21.05	24.58
630	21.14	24.67
635	21.22	24.76
640	21.30	24.85
645	21.39	24.94
650	21.47	25.03

655	21.55	25.12
660	21.63	25.21
665	21.71	25.29
670	21.79	25.38
675	21.86	25.46
680	21.94	25.55
685	22.02	25.63
690	22.09	25.71
695	22.17	25.79
700	22.24	25.88
705	22.31	25.96
710	22.39	26.04
715	22.46	26.11
720	22.53	26.19
725	22.60	26.27
730	22.67	26.35
735	22.74	26.42
740	22.81	26.50
745	22.88	26.57
750	22.95	26.65
755	23.02	26.72
760	23.09	26.80
765	23.15	26.87
770	23.22	26.94
775	23.29	27.01
780	23.35	27.08
785	23.42	27.15
790	23.48	27.23
795	23.54	27.29
800	23.61	27.36
805	23.67	27.43
810	23.73	27.50
815	23.80	27.57
820	23.86	27.64
825	23.92	27.70
830	23.98	27.77

835	24.04	27.84
840	24.10	27.90
845	24.16	27.97
850	24.22	28.03
855	24.28	28.10
860	24.34	28.16
865	24.40	28.22
870	24.46	28.29
875	24.52	28.35
880	24.57	28.41
885	24.63	28.47
890	24.69	28.54
895	24.74	28.60
900	24.80	28.66
905	24.85	28.72
910	24.91	28.78
915	24.97	28.84
920	25.02	28.90
925	25.07	28.96
930	25.13	29.02
935	25.18	29.07
940	25.24	29.13
945	25.29	29.19
950	25.34	29.25
955	25.40	29.31
960	25.45	29.36
965	25.50	29.42
970	25.55	29.48
975	25.60	29.53
980	25.66	29.59
985	25.71	29.64
990	25.76	29.70
995	25.81	29.75
1000	25.86	29.81

S.2.5. Quasi-1D plasma chemical kinetics model

The quasi-1D plasma chemical kinetics model solves the following continuity equation for all species, taking into account the production and loss terms defined by the chemical reactions:

(16)

Where $a_{ij}^{(L)}$ and $a_{ij}^{(R)}$ are the stoichiometric coefficients of species i, on the left- and right-hand side of a reaction j, respectively, n_l is the species density of the reacting species, and k_j is the rate coefficient of reaction j, which has the following general form:

(17)

Where A, B, C and D are the species, , and their stoichiometric coefficients and represents the reaction enthalpy.

Typically, the rate coefficients for the reactions between neutrals and ions (i.e., heavy particles) are obtained from literature, while the rate coefficients for the electron processes have to be calculated. This calculation is performed by the BOLSIG+ Boltzmann solver, which is built into ZDPlasKin, i.e., the solver we use for this quasi-1D model, and it requires only the electron impact cross sections. It solves the Boltzmann equation for the electrons using a two-term approximation to calculate the electron energy distribution function.

S.3. Additional experimental results

S.3.1. Distinct operation modes of the reactor

The new configuration of our RGA reactor can operate in three different modes depending on the electrical current: (i) a rotating arc of variable length (rotating arc regime), (ii) a steady arc with stable length (steady arc regime), and (iii) a transition regime in which the plasma arc always switches between the two aforementioned arc regimes.

In GA plasma reactors, a plasma arc is created in the shortest gap between cathode and anode. In typical RGA plasma reactors, the arc immediately starts gliding along the reactor body due to the swirling gas flow. One side of the arc remains attached to the top of the cathode, while the other side glides around the surface of the reactor body (anode); this results in arc elongation. While the arc is gliding, it also rotates along the internal surface of the anode.

When powered by a current source, which is the case in our setup, the elongation of the arc is represented by the nearly linear increase in discharge voltage (Figure S.5a). The discharge current decreases due to the rising arc length, and thus rising arc resistance. During arc elongation, energy is dissipated into heat and radiation. Therefore, if the supplied power is not sufficient to sustain further arc extension, the arc will extinguish, which is presented by a sudden drop of the discharge current (Figure S.5a), and a reciprocal jump in the electrode voltage. As a result, reignition will take place in the shortest gap between both electrodes. This is the common operating regime of the RGA reactor. However, if certain conditions are met, the arc can stabilize due to the intense heat transfer to the reactor walls (so-called wall stabilization). In this steady arc regime, the supplied power is high enough for the arc to elongate and reach the furthest point of contact on the reactor outlet. At this high-power level, the arc does not extinguish, and remains relatively stable in the center of the reactor with a constant length, which is reflected by the relatively constant values of discharge voltage and current (Figure S.5b).

However, this change in arc regime does not occur abruptly. In our RGA plasma reactor, when coupled with the effusion nozzle, we observed that at low power (90 to 130 W) the reactor is always in the rotating arc regime. At intermediate power (135 to 185 W), the reactor is in a transition regime: although this power is enough for elongation of the plasma arc to the furthest contact point in the reactor outlet, it is not high enough for long term stabilization of the arc, like in the steady arc regime. Therefore, the plasma arc is always switching between steady and rotating regime (Figure S.5c). Eventually, at even higher power (> 190 W) the steady arc regime is achieved.

These distinct operating regimes of our RGA reactor are also clear when we plot voltage as a function of applied current, in so-called V-I characteristics, recorded from the oscilloscope (Figure S.6Figure S.6. V-I characteristics of the RGA

reactor, operating at different currents (yielding different plasma powers). As our power supply is a current source, the supplied power can only be adjusted by changing the current. When the reactor is supplied with around 60 mA, a voltage of about 1.7 kV dissipates into the plasma (), the gas breaks down and a plasma is ignited, and the reactor starts to operate in the rotating arc regime. By increasing the current up to 80 mA, the reactor still operates in the rotating arc regime, and a higher current results in a lower voltage, characteristic for an arc plasma. Upon further increasing the current, the reactor operation mode enters the transition arc regime, which is reflected by a jump in the plasma voltage. The reactor stays in this regime up to a current of about 110 mA. As mentioned above, the plasma arc constantly switches between rotating and steady arc regime. Consequently, measuring the plasma V-I characteristics is quite difficult, which is reflected by the larger error bars determined for the measured plasma voltage. When the plasma current is above 120 mA, the plasma power is high enough () to sustain the elongated plasma arc and the reactor keeps operating in the steady arc regime.

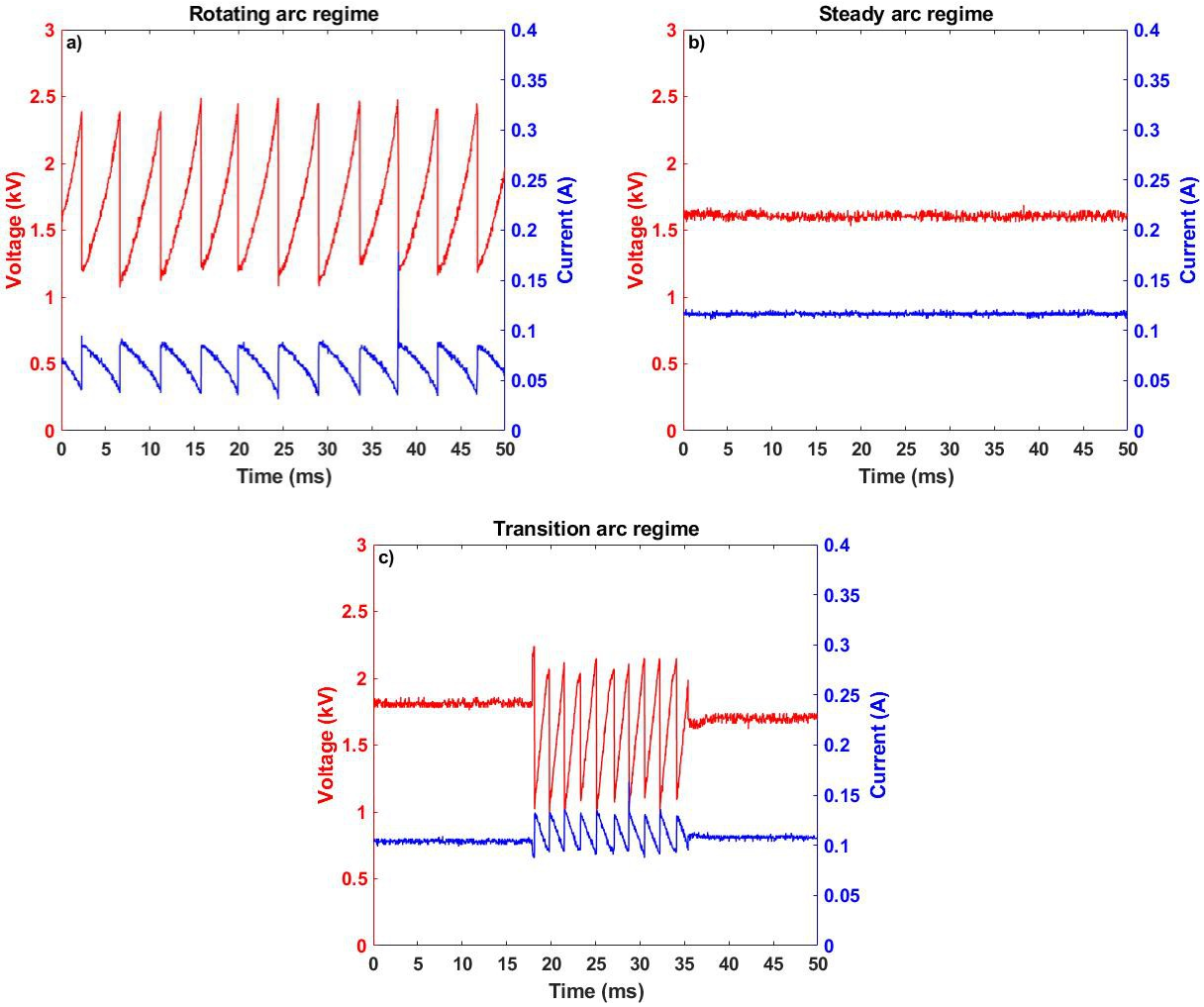

Figure S.5. Current and voltage time evolution of the plasma arc operating in a) rotating, b) steady, and c) transition arc regime, for an N_2/O_2 ratio of 50/50 and gas flow rate of 2 L/min.

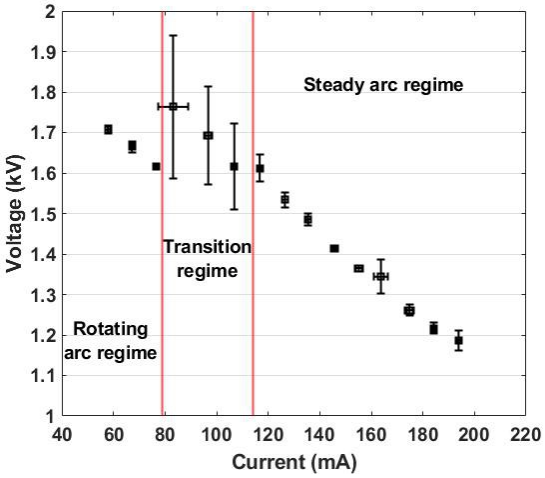

Figure S.6. V-I characteristics of the RGA reactor, operating at different currents (yielding different plasma powers) for an N_2/O_2 ratio of 50/50 and gas flow rate of 2 L/min.

S.3.2. Effect of gas volumetric flow rate on the NO_x yield and process energy cost

Error: Reference source not found compares the performance of the RGA plasma reactor with effusion nozzle at different flow rates for both rotating and steady arc regime, in terms of NO_x concentration and energy cost, as a function of N_2/O_2 ratio. It should be noted that flow rates of 1 and 1.5 L/min actually always resulted in the steady arc regime, even at low power, which normally results in the rotating arc regime. Indeed, at these low flow rates, the plasma arc could already elongate and reach the furthest point of contact at the reactor outlet. Nevertheless, the data of 1 and 1.5 L/min at these lower power values are also plotted in the figures of the rotating arc regime, to compare them with the other data at this lower power.

In both rotating and steady arc regime, the NO_x concentration decreases with increasing flow rate, due to the shorter gas residence time inside the plasma (Error: Reference source not foundа,b). In the rotating arc regime, the highest NO_x concentration of 4.7% was measured at a flow rate of 1 L/min, but the results are very similar at 1.5 L/min. In the steady arc regime, the highest NO_x concentration is about 6%, measured at a flow rate of 1 L/min, but again the results are very similar at 1.5 and even 2 L/min.

The lowest flow rates also require the lowest power to sustain the plasma, in both rotating and steady arc regime (Error: Reference source not foundе,f), but because the SEI is the ratio of power over flow rate, the energy cost is not the lowest at these low flow rates; even more, in the steady arc regime, the lowest flow rate gives rise to the highest energy cost (Error: Reference source not foundc,d). In the rotating arc regime, the lowest energy cost is 2.1 MJ/mol, at a flow rate of 1.5 L/min (Error: Reference source not foundc), while in the steady arc regime, the

lowest energy cost is 2.3 MJ/mol, at a flow rate of 4 L/min. Note however that the energy cost in the steady arc regime does not change considerably upon changing flow rate, certainly not at more O_2-rich mixtures..

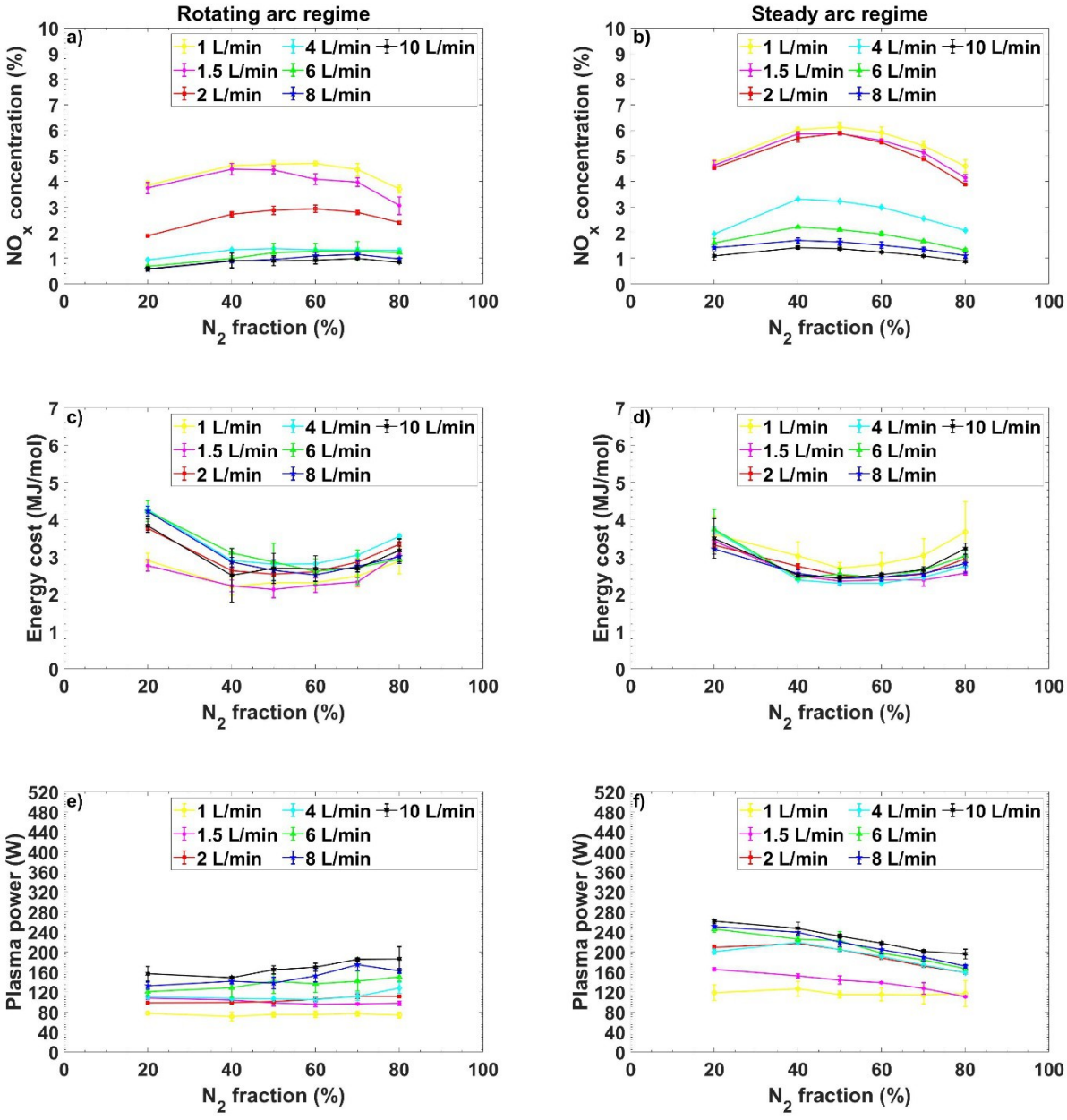

Figure S.7. Effect of total gas flow rate on the performance of the RGA reactor with effusion nozzle, in terms of NO_x yield (a, b), energy cost (b, c), and plasma power (e, f), for the rotating (left) and steady (right) arc regimes. Note: a steady arc was formed at flow rates of 1 and 1.5 L/min for the entire range of N_2/O_2 ratios, even at low power, but

these data are still plotted in the left panels, as they were obtained at similar power as the other data in the rotating arc regime.

S.4. Additional modelling results

Figure S.8 shows a close-up of the gas flow behavior inside the effusion nozzle. The gas spreads in all directions when it exits the reactor outlet, because the nozzle blocks the original flow path. The flow does not immediately exit the nozzle through the small radial holes, and some recirculation can occur (red arrow in the figure). Notice that Figure S.8 does not consider the gas divider that was shown in the nozzle geometry in Figure 2 of the main paper. This adaptation was made, based on the experimental observations, because the gas divider partially melted due to the hot temperature of the arc.

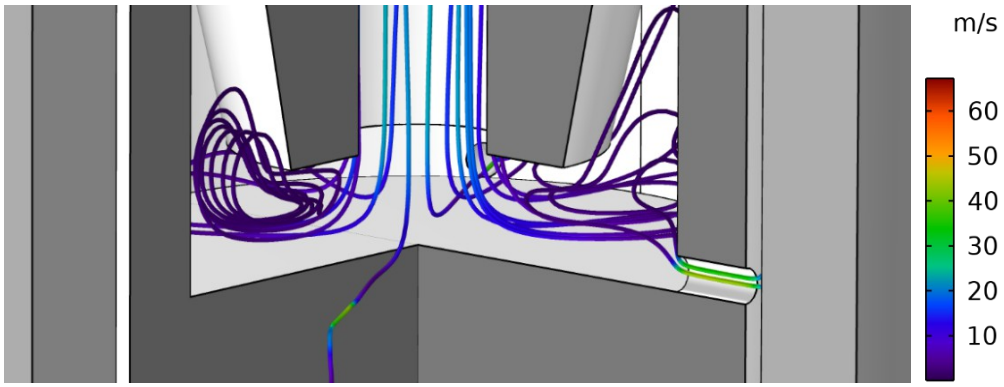

Figure S.8: Close-up of the gas flow streamlines in the effusion nozzle.

Figure S.9 illustrates the trajectories of molecules that experience a maximum temperature between 2750 and 3000 K (3000 K group; blue) and between 3750 and 4000 K (4000 K group; red). Only half of the reactor is shown, for easier visualization. Besides the fact that the “higher temperature group” flows closer to the center of the reactor than the “colder group”, we also see the recirculation of the gas, like in Figure S.8 above, see red arrow. This is interesting, since the recirculation leads to the molecules flowing for a second time close to the exit of the reactor outlet where higher temperatures are present, see Figure 9 of the main paper. This has a

minor effect on the chemistry, as it will lead to a second peak in their experienced temperature profile, see below.

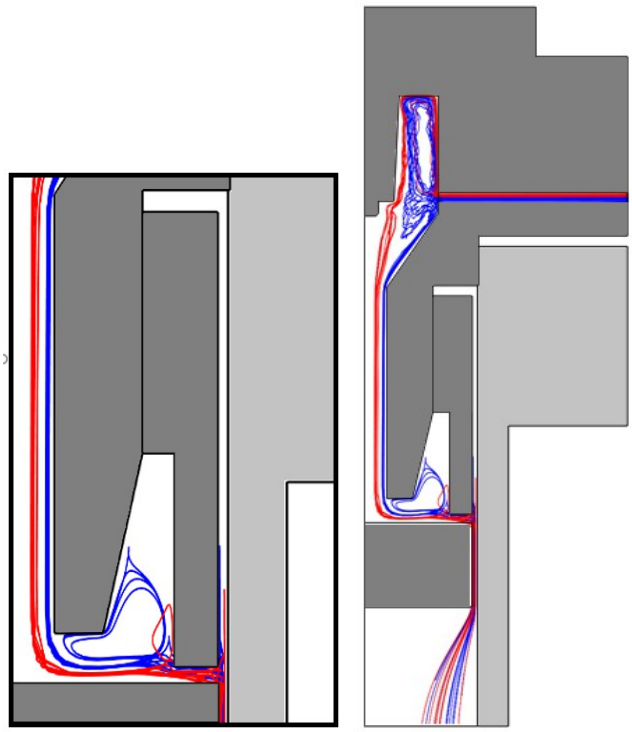

Figure S.9: Calculated trajectories of molecules that experience a maximum temperature between 2750 and 3000 K (blue) and between 3750 and 4000 K (red), in half of the reactor.

S.5. Reaction analysis for explaining the better performance of the effusion nozzle

Table S.4 presents the reaction analysis of the most important formation and destruction reactions at the time step where the NO_x concentration decreases (cf. Figure 10 in the main paper), for the 3500 K temperature group. We calculated the contribution of each reaction that forms or destroys NO or NO_2, based on its reaction rate divided by the sum of the rates of all the reactions leading to the destruction or formation of NO or NO_2:

(29)

For NO_2, the most important loss channel is the conversion of NO_2 back into NO, but as no significant contributions were found for reactions that would convert NO_2 back into N_2 and O_2, NO_2 is not the reason for the drop in total NO_x concentration. The latter is clearly attributed to NO. While part of NO is destroyed to NO_2 and hence thus not decrease the total NO_x concentration, the recombination reactions of NO with N or O atoms, back into N_2 and O_2 (i.e., the reverse processes of the Zeldovich mechanism) are responsible for the drop in NO_x concentration.

Table S.4: Most important formation and loss reactions for NO and NO_2 and their relative contributions during cooling of the gas for an N_2/O_2 feed ratio of 80/20, for the 3500 K temperature group (see details in main paper). M stands for any neutral molecule.

Formation reactions of NO	
Reaction	Contribution (%)
$NO_2 + M \rightarrow NO + O + M$	87.79
$O + N_2 \rightarrow N + NO$	6.15
$O + NO_2 \rightarrow NO + O_2$	2.29
$N + O_2 \rightarrow O + NO$	1.93
$N + O_2 \rightarrow O + NO$	1.30
$NO_2 + NO_2 \rightarrow NO + NO_3$	0.38

Destruction reactions of NO	
Reaction	Contribution (%)
$NO + O \rightarrow NO_2$	88.09
$N + NO \rightarrow O + N_2$	6.12
$O + NO \rightarrow N + O_2$	3.29
$NO + O_2 \rightarrow O + NO_2$	2.09
$NO + NO_3 \rightarrow NO_2 + NO_2$	0.34

Formation reactions of NO_2	
Reaction	Contribution (%)
$NO + O \rightarrow NO_2$	96.91
$NO + O_2 \rightarrow O + NO_2$	2.30
$NO + NO_3 \rightarrow NO_2 + NO_2$	0.74

Destruction reactions of NO_2	
Reaction	Contribution (%)
$NO_2 + M \rightarrow NO + O + M$	96.47
$O + NO_2 \rightarrow NO + O_2$	2.52
$NO_2 + NO_2 \rightarrow NO + NO_3$	0.82

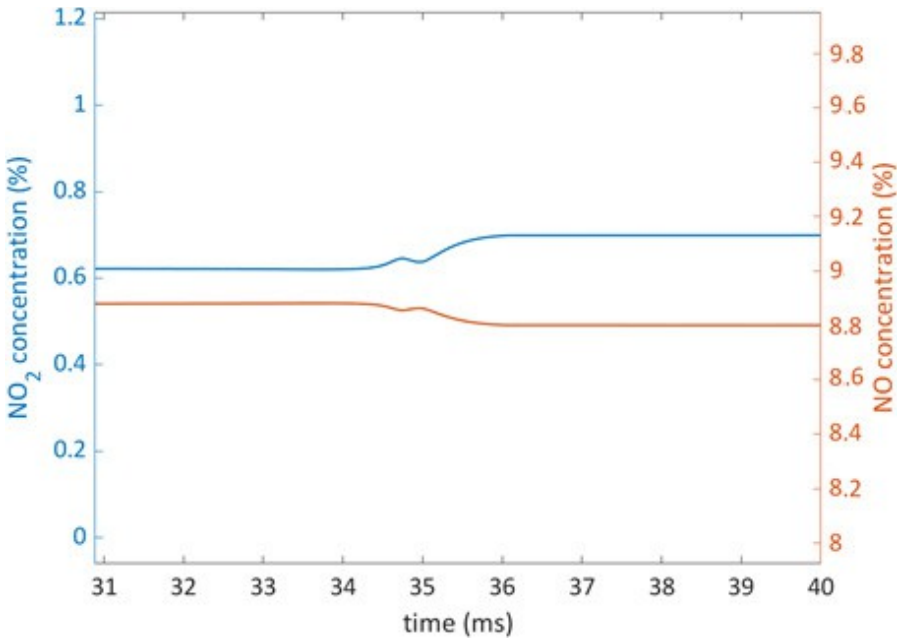

Figure S.10: Calculated NO (orange) and NO_2 (blue) concentrations as a function of time, during the second temperature peak in the 3500 K temperature group, for the effusion nozzle (see Figure 11 in the main paper).

References

[1] G. Trenchev, S. Kolev, W. Wang, M. Ramakers, A. Bogaerts, J. Phys. Chem. C 121 (2017) 24470–24479.

[2] E. Vervloessem, M. Aghaei, F. Jardali, N. Hafezkhiabani, A. Bogaerts, ACS Sustain. Chem. Eng. 8 (2020) 9711–9720.

[3] F. Jardali, S. Van Alphen, J. Creel, H. Ahmadi Eshtehardi, M. Axelsson, R. Ingels, R. Snyders, A. Bogaerts, Green Chem. 23 (2021) 1748–1757.

[4] M. Ramakers, S. Heijkers, T. Tytgat, S. Lenaerts, A. Bogaerts, J. CO2 Util. 33 (2019) 121–130.

[5] S. Van Alphen, F. Jardali, J. Creel, G. Trenchev, R. Snyders, A. Bogaerts, Sustain. Energy Fuels 5 (2021) 1786–1800.

[6] E. P.J. Linstrom and W.G. Mallard, NIST Chemistry WebBook, NIST Standard Reference Database Number 69, National Institute of Standards and Technology, Gaithersburg MD, n.d.

[7] W. Wang, B. Patil, S. Heijkers, V. Hessel, A. Bogaerts, ChemSusChem 10 (2017) 2110.

[8] (n.d.).

[9] S.W. Churchill, H.H.S. Chu, Int. J. Heat Mass Transf. 18 (1975) 1323–1329.

[10] S.W. Churchill, H.H.S. Chu, Int. J. Heat Mass Transf. 18 (1975) 1049–1053.